



LAWRENCE
LIVERMORE
NATIONAL
LABORATORY

Calculation of Mass Transfer Coefficients in a Crystal Growth Chamber through Heat Transfer Measurements

J. H. Bell, L. A. Hand

May 4, 2005

Disclaimer

This document was prepared as an account of work sponsored by an agency of the United States Government. Neither the United States Government nor the University of California nor any of their employees, makes any warranty, express or implied, or assumes any legal liability or responsibility for the accuracy, completeness, or usefulness of any information, apparatus, product, or process disclosed, or represents that its use would not infringe privately owned rights. Reference herein to any specific commercial product, process, or service by trade name, trademark, manufacturer, or otherwise, does not necessarily constitute or imply its endorsement, recommendation, or favoring by the United States Government or the University of California. The views and opinions of authors expressed herein do not necessarily state or reflect those of the United States Government or the University of California, and shall not be used for advertising or product endorsement purposes.

This work was performed under the auspices of the U.S. Department of Energy by University of California, Lawrence Livermore National Laboratory under Contract W-7405-Eng-48.

Calculation of Mass Transfer Coefficients in a Crystal Growth Chamber through Heat Transfer Measurements

James H. Bell, Lawrence A. Hand

ABSTRACT

The growth rate of a crystal in a supersaturated solution is limited by both reaction kinetics and the local concentration of solute. If the local mass transfer coefficient is too low, concentration of solute at the crystal-solution interface will drop below saturation, leading to a defect in the growing crystal. Here, mass transfer coefficients are calculated for a rotating crystal growing in a supersaturated solution of potassium di-phosphate (KDP) in water. Since mass transfer is difficult to measure directly, the heat transfer coefficient of a scale model crystal in water is measured using temperature-sensitive paint (TSP). To the authors' knowledge this is the first use of TSP to measure temperatures in water. The corresponding mass transfer coefficient is then calculated using the Chilton- Colburn analogy.

Measurements were made for three crystal sizes at two running conditions each. Running conditions include periodic reversals of rotation direction. Heat transfer coefficients were found to vary significantly both across the crystal faces and over the course of a rotation cycle, but not from one face to another. Mean heat transfer coefficients increased with both crystal size and rotation rate. Computed mass transfer coefficients were broadly in line with expectations from the full-scale crystal growth experiments. Additional experiments show that continuous rotation of the crystal results in about a 30% lower heat transfer compared to rotation with periodic reversals. The continuous rotation case also shows a periodic variation in heat transfer coefficient of about 15%, with a period about $1/20^{\text{th}}$ of the rotation rate.

NOMENCLATURE

A	Amperes
c	Concentration
C_p	Coefficient of heat at constant pressure
Ec	Eckert number
g	Body force
Gr	Grashof number
h	Heat transfer coefficient

k_c	Mass transfer coefficient
L	Length scale (width of crystal or model)
q''	Heat flux (power/area)
P	Period (also pressure)
Pr	Prandtl number
Re	Reynolds number
Sc	Schmidt number
t	Time
T	Temperature
u	Velocity
U	Velocity scale
V	Volts

Greek Symbols

ρ	Density
ν	Kinematic viscosity
ϕ	Dissipation function
ω	Crystal or model rotation rate
Ω	Maximum crystal or model rotation rate

Subscripts

F	Full-scale condition
M	Model-scale condition
S	Surface condition
∞	Bulk fluid condition

Acronyms

KDP	Potassium di-hydrogen phosphate
NIF	National Ignition Facility
TSP	Temperature-sensitive paint

INTRODUCTION

I. The NIF Crystal Growth Facility

The National Ignition Facility (NIF) at the Lawrence Livermore National Laboratory uses a set of large lasers to heat and compress test samples to conditions appropriate for the ignition of nuclear fusion reactions. The NIF uses large crystals of Potassium Di-Hydrogen Phosphate (KDP) as frequency doublers and Pockels cells. A typical crystal is shown in figure 1.

KDP crystals of this size are grown in specialized facility at LLNL. The crystals are grown in large (41" dia \times 59" high) cylindrical tanks containing a solution of KDP in water. Seed crystals are mounted on a platform which spins in the solution bath as the crystal

is grown. The platform does not spin at a constant rate. Instead it follows a rotation cycle diagrammed in figure 2. Starting from rest, the platform accelerates to a specified rotation rate, remains at that rate for a fixed time, and then decelerates to rest. After briefly pausing at zero rotation rate, the platform then follows the same spin profile in the opposite direction. The “cruise” rotation rate is 75 rpm initially, and is decreased in steps to 15 rpm as the crystal reaches its maximum size. This rotation profile has been developed through trial and error. In some cases the growing crystal develops imperfections and must be discarded. Further optimization of the rotation profile, both to improve growth rate and reduce defects, is desirable.

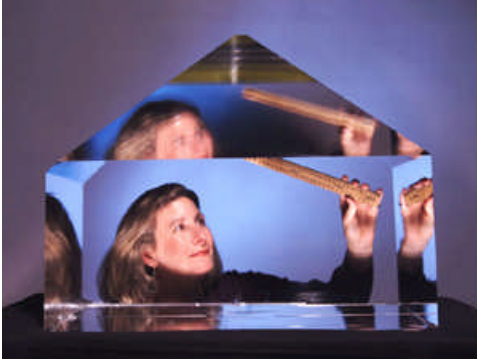


Figure 1. Photo showing a high quality 50 cm KDP crystal produced for the NIF.

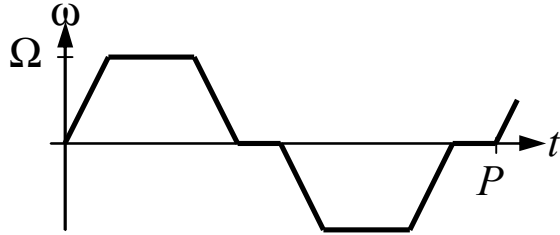


Figure 2. Notional rotation rate vs time schedule for crystal growth experiment. Ω is the maximum, or “cruise” rotation rate. The acceleration period, cruise period, and stop period are all specified as fixed fractions of the total period P .

The growth of crystals in a supersaturated solution depends on two independent factors. Reaction kinetics controls the rate at which atoms are added to the crystal. Growth must occur at the same rate across the entire crystal face. At the same time, the concentration of solute must be above the saturation level at all points on the surface. At each point on the crystal surface, growth extracts material from the solution which must be replaced by convecting/diffusing new solution to the surface. If there is insufficient convection/diffusion at a point on the surface, the solution concentration may

drop below saturation locally, causing growth to stop at that point and producing a crystal defect. The present experiment attempts to determine the mass transfer coefficient across the crystal face in order to determine if it is sufficient to allow crystal growth.

Mass transfer coefficients are difficult to measure experimentally. However heat transfer coefficient can be measured much more readily, and under many conditions heat transfer coefficient can be used to estimate mass transfer coefficient. The theoretical basis for this assertion is developed in the following section. The method for making heat transfer measurements is diagrammed in figure 3. A plastic-block scale model of a crystal is placed on a rotating platform in a scale model of the crystal growth chamber. Resistance heaters on the faces of the block generate a constant heat flux into the surrounding fluid. The surface temperature of the faces T_s is measured with temperature-sensitive paint, and the heat transfer coefficient, h is given by $h(x, y, t) = \dot{q}'' / (T_s(x, y, t) - T_\infty)$. Details of the measurements are elaborated on in the sections on equipment and experimental procedure.

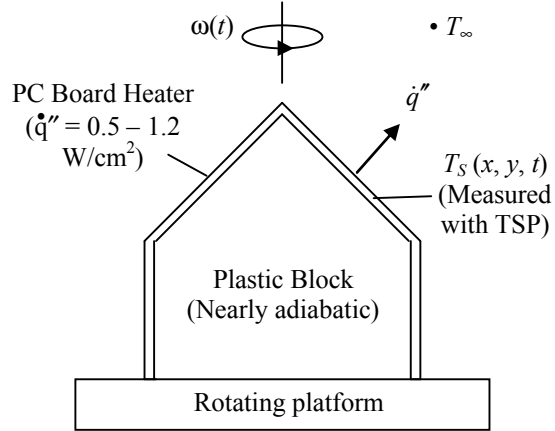


Figure 3. Diagram of heat transfer experiment. Surface temperatures are measured with temperature-sensitive paint while heated plastic model rotates at rate $\omega(t)$ in fluid with bulk temperature T_∞ .

II. Calculation of Mass Transfer from Heat Transfer Measurements

Consider two experiments. In the full scale experiment (F) a mass transfer measurement is desired while in the model scale experiment (M) a heat transfer measurement can be made. Heat transfer is governed by the non-dimensionalized equations (1) and (2), below, while mass transfer is governed by equations (3) and (4).

Heat Transfer

$$\frac{D\bar{u}^*}{Dt^*} = \frac{1}{Re} \nabla^{*2} \bar{u} - \nabla^* P^* - \frac{Gr}{Re^2} T^* \bar{g}^* \quad (\text{Momentum - 1})$$

$$\frac{DT^*}{Dt^*} = \frac{1}{Re Pr} \nabla^{*2} T^* + \frac{Ec}{Re} \Phi^* \quad (\text{Energy - 2})$$

Mass Transfer

$$\frac{D\bar{u}^*}{Dt^*} = \frac{1}{Re} \nabla^{*2} \bar{u} - \nabla^* P^* - \frac{Gr}{Re^2} c^* \bar{g}^* \quad (\text{Momentum - 3})$$

$$\frac{Dc^*}{Dt^*} = \frac{1}{Re Sc} \nabla^{*2} c^* \quad (\text{Species - 4})$$

Here \bar{u}^* , P^* , T^* , c^* , t^* are non-dimensionalized velocity, pressure, temperature, species concentration, and time, respectively. \bar{g}^* and Φ^* are the non-dimensionalized buoyancy force and dissipation function, respectively. Re , Gr , Pr , Sc , and Ec are the Reynolds, Grashof, Prandtl, Schmidt, and Eckert numbers, respectively. It should also be noted that the material derivative,

$$\frac{D\bar{u}^*}{Dt^*} = \frac{1}{St} \frac{\partial \bar{u}^*}{\partial t^*} + \nabla^* \cdot \bar{u} \quad (5)$$

contains an additional non-dimensional parameter, the Strouhal number, St . It is assumed that the heat transfer experiment is conducted in a single-species fluid, so species transfer is irrelevant, while the mass transfer experiment occurs at constant temperature, so heat transfer is irrelevant.

The heat transfer and mass transfer experiments are geometrically similar, so the boundary conditions are the same. The mass transfer experiment (F) is characterized by the nondimensional parameters St_F , Re_F , Gr_F , and Sc_F , while the heat transfer experiment (M) is characterized by the nondimensional parameters St_M , Re_M , Gr_M , Pr_M , and Ec_M . The functional forms of equations (1) and (3) would be identical if $St_F = St_M$, $Re_F = Re_M$, $Gr_F = Gr_M$. Furthermore, the functional forms of equations (2) and (4) would be identical if, in addition, $Sc_F = Pr_M$, and $(Ec/Re)_M \ll (1/Pr)_M$. If these conditions were satisfied, heat transfer in the model scale experiment would correspond exactly to mass transfer in the full scale experiment. It is worthwhile to discuss these conditions in detail, since they have important implications, and since several of them can be relaxed in practice.

$St_F = St_M$, $Re_F = Re_M$: Reynolds number matching is the *sine qua non* of fluid mechanics experiments, since it matches the ratio of inertial and viscous forces. The requirement to match Strouhal number arises because the crystal platform periodically reverses its direction of rotation, as shown in figure 2, thus introducing a

frequency constraint which must be followed. If the crystal is characterized by a length scale L , the requirements $St_F = St_M$, $Re_F = Re_M$, amount to requiring that

$$\frac{\Omega_M}{\Omega_F} = \frac{L_F^2}{L_M^2} \frac{v_M}{v_F} \quad \frac{P_M}{P_F} = \frac{\Omega_F}{\Omega_M} \quad (6)$$

where v_F and v_M are the kinematic viscosities of the fluids used in the full scale and model scale cases, respectively. Note that the required rotation rate in the model scale experiment increases quadratically with the ratio of the length scales, while the period of the rotation cycle decreases quadratically with the same parameter. Therefore, the angular acceleration rate of the model crystal increases as the fourth power of the scale factor. This turns out to be an important constraint on the model experiment apparatus.

$Gr_F = Gr_M$. This ensures that buoyancy effects, and the ratio of free to forced convection, will be the same for both the model and full scale experiments. Exact matching of Grashof numbers between the model and full scale cases is difficult because this term is dependent on many experimental parameters. However, if both the model and full scale Grashof numbers are small compared to the Reynolds number, then the buoyancy terms in both equations (1) and (3) will be negligible compared to the other terms and can be ignored. Thus the requirement that $Gr_F = Gr_M$ is replaced with $Gr_F/Re^2 \ll 1$ and $Gr_M/Re^2 \ll 1$ (Re already having been matched for the two cases.) Fortunately this is true in the present experiment. In addition, no detectable change has been noted in CFD simulations of the crystal experiment with buoyancy terms turned on and off.¹

$(Ec/Re)_M \ll (1/Pr)_M$. Fortunately the Eckert number is generally quite small compared to the Reynolds number, so in the present experiment this condition holds.

$Sc_F = Pr_M$. Equating the Schmidt and Prandtl numbers scales the diffusional boundary layer to match the thermal boundary layer. These coefficients are controlled by fluid properties and are in general quite difficult to match. In the present experiment, for example, $700 < Sc_F < 2500$ while $3.5 < Pr_M < 5.8$, depending on conditions. An alternative approach employed in the present study is to use the Chilton-Colburn analogy to relate heat transfer values in the model scale to the mass transfer values expected in the full scale experiment. The Chilton-Colburn analogy is based on the empirical observation that

$$\left[\frac{h}{\rho C_p U} (Pr)^{1/3} \right]_M = \left[\frac{k_C}{U} (Sc)^{1/3} \right]_F \quad (7)$$

where h and k_C are the heat and mass transfer coefficients, respectively, ρ is fluid density, C_p is coefficient of heat at constant pressure, and U is fluid velocity. If the Reynolds numbers of both experiments are matched, then the two fluid velocities can be related by

$$\text{Re}_M = \text{Re}_F \Rightarrow \left(\frac{UL}{\nu} \right)_M = \left(\frac{UL}{\nu} \right)_F \quad (8)$$

and so equation (7) can be rewritten as

$$\frac{k_{CF}}{h_M} = \frac{1}{(\rho C_p)_M} \frac{L_M \nu_F}{L_F \nu_M} \left(\frac{\text{Pr}_M}{\text{Sc}_F} \right)^{2/3} \quad (9)$$

or, alternatively,

$$\frac{k_{CF}}{h_M} = \frac{L_M D_F}{L_F k_F} \left(\frac{\text{Sc}_F}{\text{Pr}_M} \right)^{1/3} \quad (10)$$

where D_F and k_F are the mass transfer diffusion coefficient and heat conductivity, respectively, of the full scale fluid. The Chilton-Colburn analogy has been experimentally verified over a range of $0.6 < \text{Pr} < 60$ and $0.6 < \text{Sc} < 3000$, which encompasses the Prandtl and Schmidt number ranges of the present experiment. However, the authors know of no study which has verified the Chilton-Colburn analogy for rotating

systems.

III. Temperature-Sensitive Paints

In the present experiment, heat transfer coefficients were deduced from instantaneous temperature measurements on the surface of a model crystal subject to uniform heating from the interior. Surface temperature measurements were made with temperature-sensitive paint, some properties of which are briefly described below.

There exist a broad range of luminescent materials whose light emission (in response to excitation with the appropriate light frequency) is dependent on temperature. Further details of this phenomenon are well-covered in several review papers^{2,3}. To first order, the brightness of a TSP is exponentially sensitive to temperature, i.e., as

$$\frac{I_1}{I_2} = e^{A(T_1 - T_2)} \quad (11)$$

where I_1, I_2 are the light intensities emitted at temperatures T_1, T_2 , respectively, and A is a sensitivity

Full-Scale Case	Crysal Size (cm)	Kinematic Viscosity (m ² /s)	Acceleration (rpm/min)	Max Velocity (rpm)	Rotation Cycle Period (s)	Reynolds Number	Strouhal Number
1F	30.0	1.02×10 ⁻⁶	500	50	68	74,000	0.0176
2F	30.0	1.02×10 ⁻⁶	500	75	68	111,000	0.0118
3F	60.0	1.40×10 ⁻⁶	200	15	56	64,000	0.0714
4F	60.0	1.40×10 ⁻⁶	200	35	56	150,000	0.0306
5F	15.0	1.02×10 ⁻⁶	500	50	68	18,000	0.0176
6F	15.0	1.02×10 ⁻⁶	500	75	68	28,000	0.0118
Model Scale Case							
1M	14.5	0.56×10 ⁻⁶	3540	133	25.5	83,000	0.0177
2M	14.5	0.56×10 ⁻⁶	3540	200	25.7	124,000	0.0117
3M	29.0	0.94×10 ⁻⁶	1490	41	20.4	61,000	0.0717
4M	29.0	0.94×10 ⁻⁶	1490	95	20.4	142,000	0.0310
5M	29.0	0.94×10 ⁻⁶	0	113	∞	168,000	0.0
6M	14.6	0.56×10 ⁻⁶	2780	118	28.9	74,000	0.0176
7M	14.6	0.56×10 ⁻⁶	2780	177	28.9	111,000	0.0117
8M	7.4	0.56×10 ⁻⁶	2550	113	30.1	18,000	0.0176
9M	7.4	0.56×10 ⁻⁶	2550	169	30.1	28,000	0.0118
10M	7.4	0.56×10 ⁻⁶	0	113	∞	18,000	0.0

Table 1. Operating conditions for both full-scale and model scale experiments. Model scale experiment is designed to match full scale Reynolds and Strouhal numbers. Model and full scale cases match as follows: 1M↔1M, 2M↔2F, 3M↔3F, 4M↔4F, 6M↔1F, 7M↔2F, 8M↔5F, 9M↔6F. For cases, 5M, 10M, see section XX.

coefficient. Typically luminescence brightness decreases with temperature, so A is generally negative. Equation (10) can also be written as

$$\frac{I_1}{I_2} = (1 + k)^{(T_2 - T_1)} \quad (12)$$

where k is understood as a (generally positive) sensitivity coefficient. In this formulation the material's temperature sensitivity is naturally expressed in terms of a fractional change in brightness per degree of temperature change. To measure temperature, the luminescent material is mixed into a coating which can be applied to the surface of interest. The painted surface is then illuminated with excitation light and two images are taken – one with the surface at a known reference temperature and the other with the surface at the unknown test condition.

EQUIPMENT

The model scale crystal experiment must match the operating conditions of the full scale crystal growth chamber for the six cases of interest summarized in table 1. The requirement to match Reynolds and Strouhal numbers imposes important constraints on the design of the model scale experiment. Water is the natural choice for the working fluid in the model scale experiment, and the high rotational velocities and accelerations which occur at model scales much below $\frac{1}{2}$ present several design problems. The higher rotation rates would require sub-millisecond flash durations to properly freeze the model in the TSP images. Also, more frictional heat would have to be dissipated in a smaller volume of water, adding another significant heat source besides that from the surface heaters. Thus it was decided to construct the model scale crystal growth tank at $\frac{1}{2}$ the full scale size, using water as the working fluid. Some thought was given to building a smaller scale model using heavy gas as the working fluid, but this approach was rejected due to the greater sealing difficulties and general inconvenience of using heavy gas instead of water.

I. Crystal Growth Chamber Model

A roughly $\frac{1}{2}$ scale model (actually 49.4%) of the LLNL crystal growth facility was constructed, as illustrated in figure 4. Figure 5 shows photographs of the model indicating its major components. The design philosophy was to reproduce the LLNL growth chamber's physical parameters as closely as practical, while maximizing optical access and allowing model heating. The model crystal growth chamber consists of four parts: the tank itself, the tank support assembly, the model platform, and the motor mount. The optical system, consisting of the TSP camera and flashlamps, is fixed to the same base as the model crystal growth chamber. The

components of the model growth chamber are described separately below.

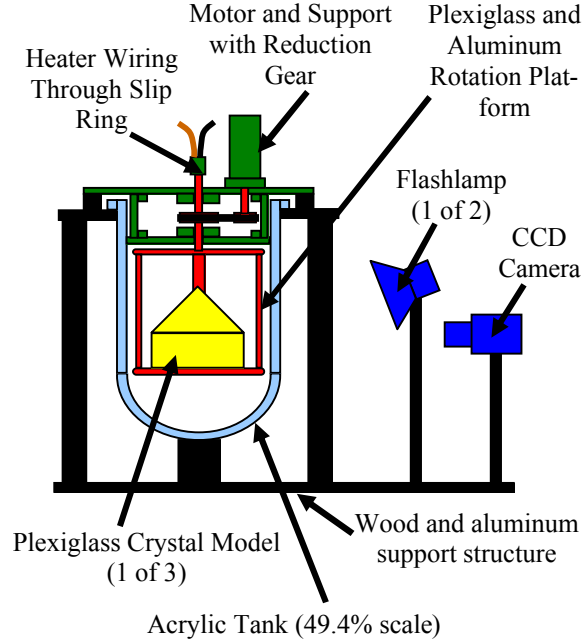


Figure 4. Side view diagram of model crystal growth chamber showing support structure, tank, optical system, crystal platform, drive motor, and crystal model.

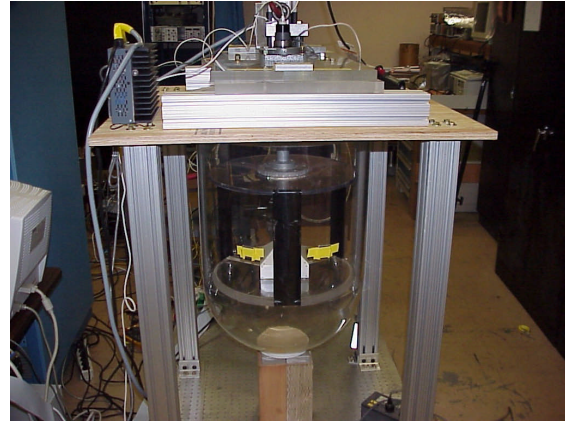


Figure 5(a). Rear view of model crystal growth chamber showing tank, support structure, and rotation stage with small crystal model. Rotation stage fins are painted black. Yellow tape holds intensity calibration coupons.

One significant difference is that the LLNL facility has a free fluid surface, while that of the model chamber can be restrained by an acrylic top. Despite its relatively large scale, the higher rotation rate of the model crystal does lead to a significantly larger amount of surface displacement in the model system compared to the LLNL facility. It was not clear initially whether restraining the surface displacement with a solid

boundary would be a less significant change than allowing a free surface with greater displacement. Once the model was constructed, visualization of the flow indicated that the closest match to the full scale facility was obtained by keeping the acrylic top right at the water surface.

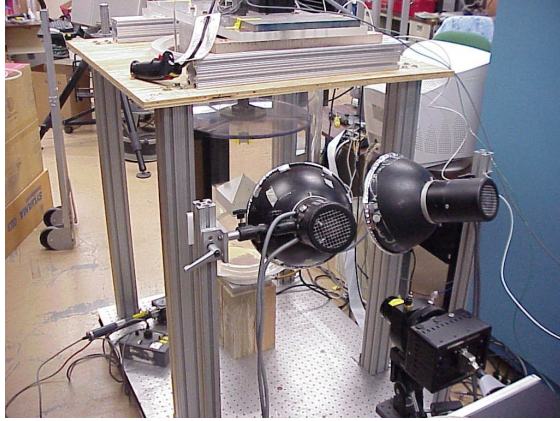


Figure 5(b). Front view of model crystal growth chamber showing flashlamps and camera in foreground.

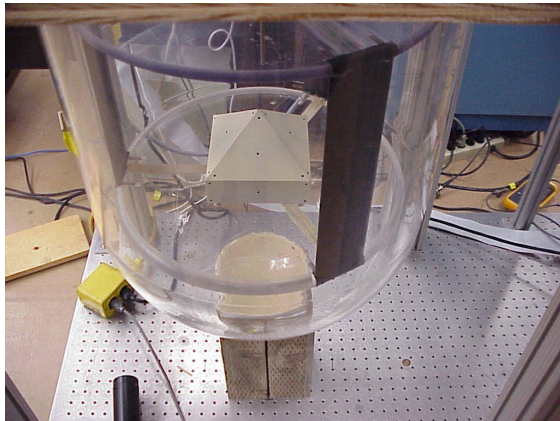


Figure 5(c). Side view of model crystal growth chamber looking down. Image shows small crystal model on rotation stage. Bottom tank support is visible beneath.

Tank. The tank is made from clear acrylic and consists of a cylindrical section of 20" outside diameter, 20" height, and 3/8" thick, attached to a matching hemispherical base. The hemispherical base is blown from 1/2" thick acrylic. The blowing process reduces the thickness of the hemispherical section to roughly 3/8" at the edges. The base is cemented to the cylinder section and the interior is polished to produce a smooth join between the sections. A ring is cemented to the top of the cylindrical section of the tank to act as a lip. Figure 6 shows a cross-section of the tank giving its dimensions.

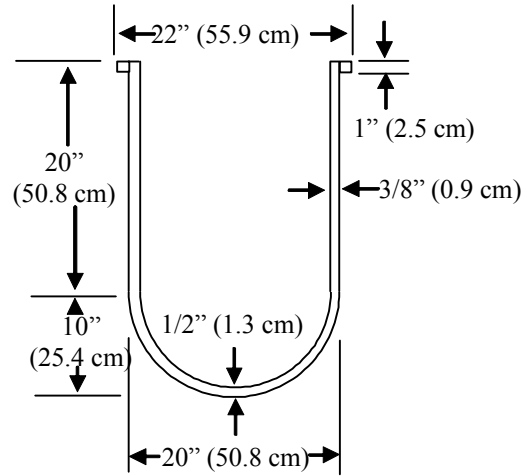


Figure 6. Cross section of model crystal growth tank.

Tank Support Assembly: The tank support consists of a 3 ft \times 3 ft (91.44 cm \times 91.44 cm) square piece of plywood with a 20 in hole in the center, which supports the tank by its lip. The plywood collar is itself supported by four aluminum columns which are mounted to an optics table. The optics table also serves as a base for mounting the camera and flashlamps. In addition to the plywood collar, the tank is also supported at the base of the hemispherical section. This support is necessary because the cemented joint between the hemispherical and cylindrical sections cannot support the weight of water when the tank is filled.

Model Platform: This assembly consists of two 17.5" acrylic disks joined by three fins, as shown in figure 6. The lower disk is thicker than the upper disk to match the full scale platform. The aluminum fins are mounted at 120° intervals. The fins have an elliptical cross section to minimize drag irrespective of rotation direction. The top disk is attached to a hollow aluminum shaft which is turned by the motor. The bottom disk has a pattern of bolt holes which allow crystal models of different sizes to be mounted to the platform. In theory the model could be mounted to the platform at any angle. In the full scale crystal growth chamber, however, seed crystals are always four-sided, and always mounted so that one side directly faces a fin. Model crystals followed this practice.

The platform contains wiring for power and/or signal transfer. Each fin has a channel cut in it for wiring, and each plate has three channels leading from the center to the fins at the edges. Wires can be routed from the crystal mount at the center of the lower disk through the fins and along the upper disk to the hollow drive shaft. The wiring channels were sized to allow the installation

of up to 12 strands of 10 gauge wire. Currently 6 strands of 12 gauge wire are installed. The grooves are filled with fiberglass putty to hold the wires in place and present a smooth surface to the flow. A Mercotac slip ring mounted on top of the hollow shaft provides electrical continuity despite the platform's rotation.

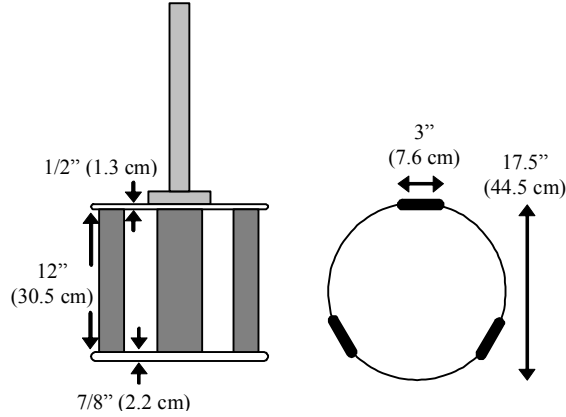


Figure 7. Side and top views of rotation platform.

Motor. The platform is spun by a Parker Compumotor TS 42B stepper motor, rated at up to 400W and 16 N-m of torque. The motor turned the platform through a 3:1 reduction gear using a toothed belt. The motor drive has a digital interface and can accept arbitrary motion control instructions. An optical encoder mounted on the motor drive shaft was used to monitor the position of the rotation platform. The precise speeds and timings of the platform rotation were determined by a motion control program running on a personal computer. This program also controlled the operation of the flashlamps and camera.

II. Crystal Models

Three crystal models were made; each following the same construction procedure. The actual crystals grown at LLNL vary considerably in shape.⁴⁵ However only a single, representative shape was chosen for the present experiment. This shape is parametrically defined as shown in figure 8. Thus the three models are geometrically similar and differ only in scale. The models are sized to represent 15, 30, and 60 cm full scale crystals.

Each model is built from an acrylic core, with each face of the core covered by a thin heater board. The cores are made slightly undersized to accommodate the additional thickness of the heater boards. The cores have hollow centers which serve as wiring compartments.

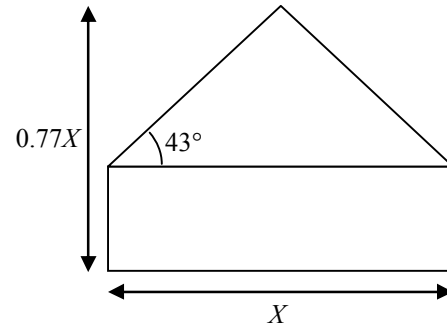


Figure 8. Side view of crystal model showing shape parameters. For a given base width, X , the total model height is 77% of X . Pyramid facets are set at an angle of 43° to the horizontal.

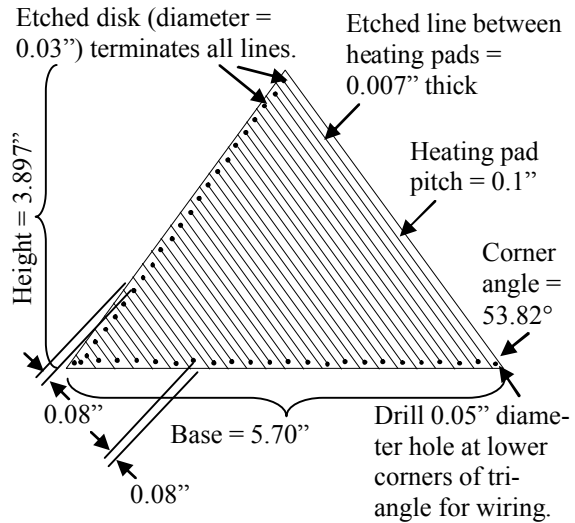


Figure 9. Heater board etching pattern for triangular face of 30 cm scale crystal model. Trace width is fixed. Number of traces varies with board size. Holes in lower corners allow wiring through back of heater board.

The heater boards are made from thin FR4 circuit board material coated on one side with copper, on which traces are etched in a serpentine pattern. Figure 9 shows a typical etching pattern, in this case for a pyramid face on the 30 cm scale crystal model. A trace pitch of 0.1" was maintained for all heater boards, so the number of traces varies with the size of the board. Prism boards are similar to the pyramid board shown in figure 9. Two sets of heater boards were manufactured. The first set included heater boards to cover the 30 and 60 cm scale models. These boards were made using 0.008" thick FR4 circuit board with 0.00017" thick copper traces. The boards displayed a tendency to burn out at the wiring contact points while under load. A plot of current equipotential lines showed that there was a

tendency for the current flux to become concentrated at the edges of the board, where it must make a 180° turn to follow the serpentine path of the trace. Later, a second set of heater boards were made to cover the 15 cm scale model, as well, as well as the 30 cm scale model for additional experiments. For the second set of boards, etched disks were added at the ends of the lines between the traces, and the copper thickness was doubled* to 0.00035". No burnouts occurred with this set of boards.

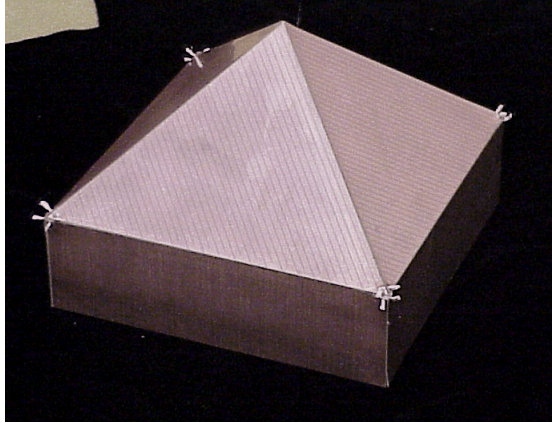


Figure 10. 30 cm crystal scale model with heater boards attached. Serpentine pattern can be seen on faces. Power leads are attached to inward-facing sides of boards at corners. Leads through holes in plexiglass core to inner wiring space. Protruding ends of power leads are visible at corners of model. These are trimmed before painting with TSP.

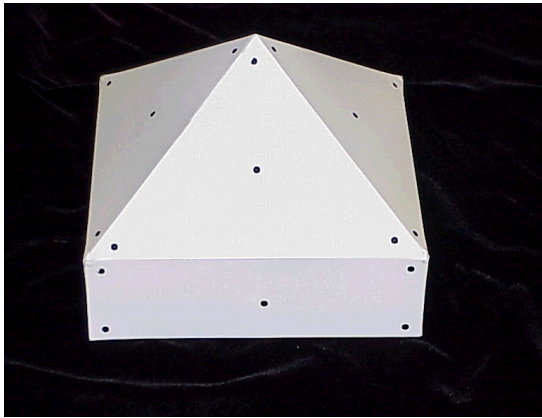


Figure 11. 30 cm crystal scale model after application of TSP. Black dots are fiducial marks for photogrammetry.

* Actual copper thicknesses were specified in industry-standard units of ounces of copper per square foot of area. Thicknesses of 0.00017" and 0.00035" correspond to 1/8 and 1/4 oz Cu / sq ft, respectively.

Power leads were wired to the back sides of the heater boards through small holes drilled in the boards at the endpoints of the serpentes. The boards were then glued to the faces of the acrylic cores using contact cement. Figure 10 shows the 30 cm scale model crystal with the heater board faces attached. Once the boards have been attached to the core, the model can then be painted with TSP as shown in figure 11.

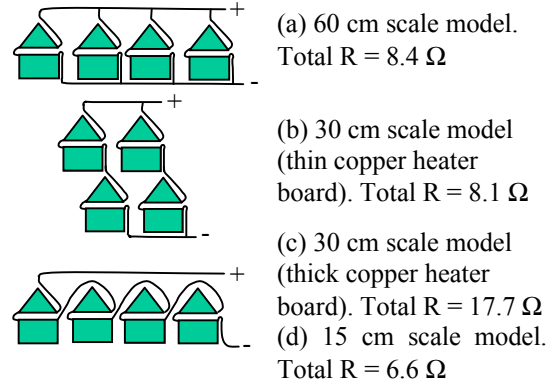


Figure 12. Wiring configurations used for crystal models, and total resistance of heater boards.

The heater boards were driven by an available 0-130 V, 20 A, AC power supply. Within the model, it is possible to wire the individual heater boards in series, parallel, or any combination. The wiring patterns and total resistance values for the three models (including both sets of heater boards for the 30 cm scale model) are shown in figure 12. Generally speaking, one would like to have the widest possible range of available heating power, which in turn implies an optimum total resistance of $130/20 = 6.5 \Omega$. The first set of heater boards for the 30 and 60 cm scale models were wired to most closely approach the optimum total resistance. The second set of heater boards for the 15 and 30 cm scale models were wired in series to simplify installation. For the 15 cm scale model, series wiring gives nearly optimum resistance. For the 30 cm scale model, sufficient power was available even with a non-optimal resistance.

III. Camera and Lamp System

Camera. A cooled CCD (charge-coupled device) camera based on a Roper Scientific ST-138 controller and SITe 1024 CCD was used in this experiment. The 1024×1024 pixel, back-thinned CCD has a high quantum efficiency of nearly 80% and a high full-well capacity of roughly 300,000 photoelectrons. A 16-bit ADC can read out the CCD at about 430 kilo-samples/sec. The camera lens was equipped with a bandpass interference filter (passband = 620 nm, full-width half-maximum = 10 nm) chosen so that the passband of the filter matched the emission peak of the TSP. The camera has a frame rate of 1/3 seconds. A

50mm f1.4 lens was used for cases 1M - 5M. An 85 mm f1.8 lens with a macro ring was used for cases 6M - 7M, and a 135 mm f2.8 lens, also with a macro ring, was used for cases 8M - 10M. Lens apertures varied from f4 to f8 during the experiments. The camera is a frame transfer camera, with light access to the CCD being controlled by a mechanical shutter with an opening time of about 15 milli-seconds – too slow to freeze the motion of the platform.

The flashlamp consisted of a single Norman 4000 Joule flash power supply driving two lamp heads. Each lamp head was driven at 1000 Joules. Flash duration at this power rating was specified by the manufacturer to be 4 milliseconds. Each flashlamp was equipped with a tempered Schott glass BG-25 filter to absorb light emitted by the lamp at the paint emission wavelength, while transmitting light at the paint excitation wavelength. The flashlamp power supply requires 7 seconds to recycle.

Image acquisition timing was determined by a motion control program running on a personal computer. As originally set up, the computer simply issued a command to take an image at the desired platform position. Since the camera shutter was much slower than the flashlamps, it was pre-opened 0.05 seconds prior to the platform reaching the desired position, and the flashlamps were fired when the shaft encoder indicated that the platform had exactly reached the chosen position. Unfortunately, the design of the motor controller resulted in all commands having a timing uncertainty of up to two clock cycles, i.e. 0-4 milliseconds. Therefore an optical system was used to fire the flashlamps. A laser and photodiode were mounted on the exterior of the tank, while a piece of retro-reflective tape was attached to the platform. When the platform reached the correct position the tape was illuminated by the laser, and the photodiode closed a switch to fire the flashlamps. The original firing command was modified for use as an arming command to prevent inadvertent operation of the flashlamp.

IV. Temperature-Sensitive Paint

Two TSP formulations were used in the present study. The first consisted of Europium III thenoyltrifluoroacetate (EuTTA) in clear model airplane dope. This combination had been used previously in air tests. It was known to be durable, waterproof, and relatively sensitive to temperature, with typical sensitivities of around $k=0.039$ at room temperature. The TSP was applied on top of a base coat which consisted of white model airplane dope. This paint was applied to the 30 cm scale model for initial testing. However, this paint

showed a tendency to delaminate from the model surface after prolonged soaking in water. Delamination was prevented by limiting the amount of time the model was left in the tank. Subsequent tests of the crystal models, including the second round of testing the 30 cm scale model, used a different paint. The second paint consisted of EuTTA in DuPont ChromaClear, which is an automotive clear coat. This paint was applied on top of a white automotive base coat. The ChromaClear-based paint proved to be much more water resistant than the dope-based paint. No deterioration of this paint was observed despite maintaining the models in the tank for several days. The sensitivity of both paints in water was less than their typical sensitivity in air. Paint calibrations (detailed in the section on experimental procedures) indicated sensitivity coefficients of $k=0.02-0.03$. The reason for the lower sensitivity in water is not known.

EXPERIMENTAL PROCEDURE

Correspondence between model and full scale cases.

Once the model scale facility was constructed, data were acquired at a variety of conditions intended to match the full scale operating conditions shown in table 1. These model scale operating conditions are also shown in table 1. Model scale cases 1M - 4M were acquired first, and were intended to match full scale cases 1F - 4F. Unfortunately, burn-outs in the heater boards limited the amount of data which were obtained in cases 1M and 2M. There was some interest in seeing the heat transfer for a case with constant rotation, and so model scale case 5M was acquired with the platform rotating at a constant rate. The results from cases 1M - 5M were considered sufficiently interesting to pursue further experiments. After redesigning the heater boards to eliminate burn-outs, cases 1M and 2M were repeated as cases 6M and 7M. New cases 8M and 9M were added to match full scale cases 5F and 6F. Finally, a second constant rotation case, 10M, was acquired. Constant rotation cases were run in both clockwise and counter-clockwise directions with no discernable difference.

Data acquisition at elevated temperature. Model scale cases 1M, 2M and 6M - 10M were conducted in water at an elevated temperature. The rationale for this procedure was to take advantage of the reduction of water viscosity with temperature to reduce the rotation rate required in the model scale experiments. By heating the water to a mean of 47.5° C, the maximum rotation rate required was reduced from roughly 300 rpm to 177 rpm. High temperature data acquisition was accomplished by first heating the water to 50° C with a heating element prior to placing the model in the tank.

Data acquisition was begun when the water temperature had cooled to 49° C, and terminated at a water temperature of 46° C. Unfortunately, an incorrect calculation of water viscosity for cases 1M and 2M lead to these cases being conducted at a slightly higher than desired rotation rate; cases 1M and 2M only approximately match the Reynolds numbers of cases 1F and 2F.

General data acquisition procedure. Data acquisition typically began with the model and rotation platform being inserted into the tank. The model was first spun through several rotation cycles over the course of five to ten minutes to dislodge bubbles in the flow and to allow the model to equilibrate to the water temperature. Once the model had been equilibrated it was spun through several rotation cycles with the heater boards turned off, during which time temperature-sensitive paint reference images were acquired. The flashlamp illumination served to freeze the model motion. The heater boards were then turned on, and the model spun through three cycles to equilibrate the flow in the heat-on condition. Finally, the model was spun through several cycles as TSP test images were acquired.

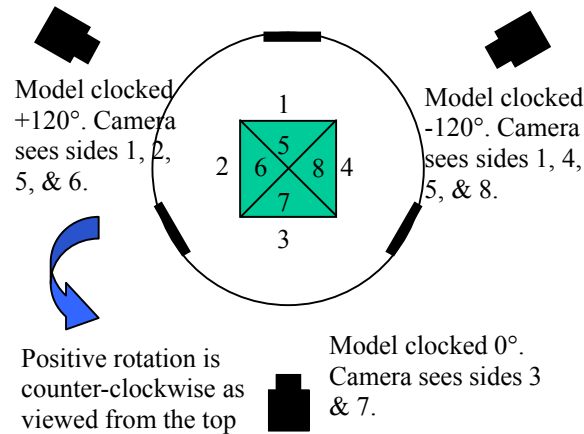


Figure 13. Model is best viewed from between fins. With only one camera, the model must be rotated (clocked) prior to running to view the desired faces. Pyramid and prism faces are numbered separately.

Limitations on viewing angle and image acquisition. In general, it was expected that heat transfer rates would vary during a cycle, with heat transfer being lowest when the platform was stopped and higher when the platform was accelerating to its “cruise” rotation rate. Ideally images should be taken at as many points during the rotation cycles as possible. Unfortunately, as shown in figure 5, the crystal model is best viewed from the sides of the tank, and indeed the camera is set up to view the model from such a position. Since there is only one camera, images can be taken only over a

restricted set of phase angles. In the present experiment, images were only taken at a 0° phase angle. In order to get images of all four sides of the model, the platform was clocked $\pm 120^\circ$ prior to starting a set of cycles, as shown in figure 13. This was equivalent to rotating the camera $\pm 120^\circ$ around the spin axis of the platform.

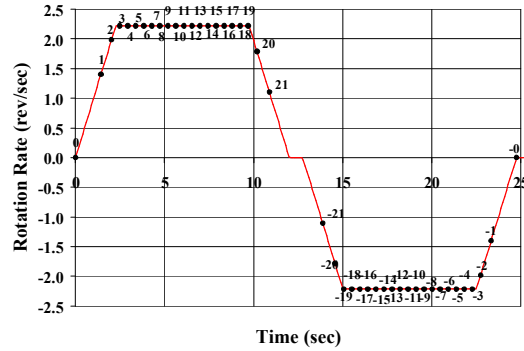


Figure 14. Rotation rate vs time for one cycle in cases 1M, 6M, and 8M. Numbered points indicate times at which the platform has rotated 360°. Points are assigned negative numbers when platform is rotating in negative direction.

The requirement that all images must be taken at 0° phase angle places limitations on where in a rotation cycle data can be acquired. Figure 14 illustrates this restriction with a plot of platform rotation rate vs. time, similar to figure 2. However in figure 14, all the points at which the platform has executed an integral number of revolutions (and thus has 0° phase angle) are marked and numbered. Starting at zero revolutions, the platform accelerates to its cruise rotation rate within three revolutions, and continues at that rate for 16 more revolutions. It decelerates to zero speed after slightly more than 21 revolutions total, and then reverses direction. The number of revolutions made by the platform varies with the cruise rotation rate and total period, and is different for each case.

Detailed data acquisition sequence. The recycle time of the flashlamp power supply sets an upper limit at the rate at which images can be acquired. Consequently, not all the desired images can be acquired in a single cycle of the platform. Instead, images are taken at staggered intervals over several cycles. For example, the complete data acquisition process for case 1M, 6M, or 8M, would be as follows:

1. Spin the platform through three rotation cycles with the heater off to establish the flow in the tank. Warm the flashlamps by firing them twice per cycle, to minimize intensity variations between subsequent flashes.

2. Spin the model through five rotation cycles, taking TSP reference images at selected 360° intervals but at staggered rotation values. Take images as follows:
 - a. Cycle 1: Rotations 0, 15, -14
 - b. Cycle 2: Rotations 1, 16, -13
 - c. Cycle 3: Rotations 2, 17, -12
 - d. Cycle 4: Rotations 3, 18, -11
 - e. Cycle 5: Rotations 4, 19, -10
3. Repeat steps 1 and 2 with heater on to acquire TSP test images.
4. Repeat steps 1 – 3, but take images at the following rotation values instead of the original values:
 - a. Cycle 1: Rotations 5, 20, -9
 - b. Cycle 2: Rotations 6, 21, -8
 - c. Cycle 3: Rotations 7, -21, -7
 - d. Cycle 4: Rotations 8, -20, -6
 - e. Cycle 5: Rotations 9, -19, -5
5. Repeat steps 1 – 3, but take images at the following rotation values instead of the original values:
 - a. Cycle 1: Rotations 10, -18, -4
 - b. Cycle 2: Rotations 11, -17, -3
 - c. Cycle 3: Rotations 12, -16, -2
 - d. Cycle 4: Rotations 13, -15, -1
 - e. Cycle 5: Rotations 14, -14, -0
6. Clock the platform +120° to view the model from one side, and repeat steps 1 – 5.
7. Clock the platform -120° to view the model from the opposite side, and repeat step 6.

Note that one rotation point (-14) is acquired twice. Also note that rotation points 0 and -0 are not identical. The model “parks” briefly at this point and pauses before the beginning of the next cycle. The stagger pattern of rotation points for the different cases is given in table 2.

In the constant rotation rate cases (5M, 10M), images were taken as follows.

1. Spin the platform through 30 rotations cycles with the heater off to establish the flow in the tank. Warm the flashlamps by firing them every 10 rotations.
2. Continue to spin the model for another 100 rotations, taking a reference TSP image every 10th rotation.
3. Repeat steps 1 and 2 with the heaters on to acquire the TSP test images.
4. Clock the platform +120° to view the model from one side, and repeat steps 1 – 3.
5. Clock the platform -120° to view the model from one side, and repeat step 4.

	1M, 6M, 8M	2M, 7M, 9M	3M	4M
1a	0, 15, -14	0, 19, -19	0, 4, -3	0, 6, -5
2a	1, 16, -13	1, 20, -13	1, 5, -2	1, 7, -4
3a	2, 17, -12	2, 21, -12	2, -5, -1	2, 8, -3
4a	3, 18, -11	3, 22, -11	3, -4, -0	
5a	4, 19, -10	4, 23, -10		
1b	5, 20, -9	5, 24, -9		3, -8, -2
2b	6, 21, -8	6, 25, -8		4, -7, -1
3b	7, -21, -7	7, 26, -7		5, -6, 0
4b	8, -20, -6	8, 27, -6		
5b	9, -19, -5	9, 28, -5		
1c	10, -18, -4	10, -28, -4		
2c	11, -17, -3	11, -27, -3		
3c	12, -16, -2	12, -26, -2		
4c	13, -15, -1	13, -25, -1		
5c	14, -14, -0	14, -24, -0		
1d		15, -23, -4		
2d		16, -22, -3		
3d		17, -21, -2		
4d		18, -20, -1		
5d		19, -19, -0		

Table 2. Rotation stagger schedules for different cases.

TSP calibration procedure: A TSP calibration cell was constructed by placing a large water-filled beaker on a hot plate in front of the crystal growth tank, where the beaker could be viewed by the TSP camera and illuminated by the flashlamps. A 1” square TSP coupon was suspended in the beaker, and successive images were taken as the water temperature was increased. Temperature was measured with an RTD element.

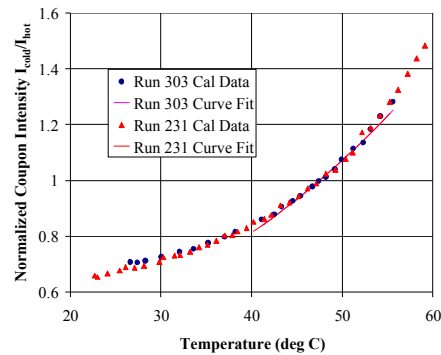


Figure 15. Coupon intensity vs water temperature for calibrations taken before and after cases 6M-10M. Intensity normalized by intensity at 47.5 °C.

Figure 15 shows the calibration curves obtained for cases 6M-10M. Data taken before and after these cases were run indicate that the TSP data are well-fit by equation 12 with $k=0.0281\pm0.0010$.

The raw TSP data were converted to heat transfer coefficients by first taking the ratio of a heat-on image with a heat-off image taken at the same point in the rotation cycle. Variations in illumination intensity from flash to flash were assessed by examining TSP coupons which were visible behind the model. The coupons were attached to the outside of the tank, with a slight stand-off to ensure they were not affected by temperature variations within the tank. The ratioed images were rescaled to ensure that the ratio of the coupon intensities was always equal to 1. Variations in flash intensity did not exceed 1%. The ratioed image was then converted to temperature by inverting equation 12, using a value of the sensitivity component determined from a coupon calibration as described in the previous paragraph. The overall model heating rate was determined by measuring the voltage across and current through the model with a precision voltmeter and ammeter. The product of voltage \times current, divided by the surface area of the model, gave the heating rate. This value was divided by the TSP-derived temperature to determine the heat transfer coefficient.

RESULTS AND DISCUSSION

Qualitative features of the heat transfer distribution: The variation of heat transfer rate across the model surface followed roughly the same pattern in all cases. Figure 16 shows the instantaneous heat transfer coefficient over side 4 for each of the 42 data points taken during case 1M. The distribution for other cases and model sides is similar. The position of each data point in figure 16 with respect to the rotation cycle is shown in figure 14. At the first points in the cycle (0,1) the heat transfer distribution is quite variable, but as the rotation rate increases (2,3) so does the overall heat transfer rate on the model. Once the rotation rate reaches its peak, a co-rotating vortex develops at the leading corner of each pyramid face. (The vortices are obvious in white-light viewing of the model due to their entrainment of bubbles.) The vortex generates regions of high heat transfer at the leading edge of each pyramid face, followed by a region of lower heat transfer due to the parcel of relatively quiescent heated fluid co-rotating with the model behind each vortex. As the model continues to rotate (4-19) this region grows in size until it encompasses nearly the entire pyramid face. The prism face is much less affected by the vortex, and does not show a significant reduction in heat transfer rate until the later rotations in the cycle (12-19). A small region of low heat transfer develops at

the leading edge of the prism face early in the rotation cycle (2-4) but is largely gone by the 12th rotation. The overall heat transfer rate drops significantly when the model begins to reverse direction (20, 21), and it backs into the already heated fluid surrounding it. Once the model has reversed direction, the heat transfer distribution is almost the opposite of that observed in the positive direction. The red area separating the pyramid and prism faces, which is indicative of very high heat transfer rate, is an artifact. Current flow at the edges of the heater boards is low, and thus the temperature difference at the board edges is low, incorrectly indicating high heat transfer.

Temporally- and spatially-averaged heat transfer rates: The time- and space-averaged heat transfer coefficient over an entire crystal face is of interest in evaluating the relative importance of reaction kinetics and local solute concentration to the crystal growth process. The averaged data also allows comparisons between cases which serve as a check on the accuracy of the measurements. Time- and space-averaged values of the heat transfer coefficient are presented in table 3.

Case	Side			
	3	4	1	2
1M	b	0.363	0.346 / 0.372	b
2M	b	b	0.389	b
3M	0.282	0.360	0.442 / 0.360	0.315
4M	0.378	0.336	0.402 / 0.456	0.386
5M	0.242	0.242	0.302 / 0.263	b
6M(1)	0.251	0.297	0.286 / 0.293	0.316
6M(2)	0.245	0.283	0.287 / 0.286	0.283
7M(1)	0.273	n/a	n/a	n/a
7M(2)	0.264	n/a	n/a	n/a
8M(1)	0.206	0.261	0.234 / 0.222	0.203
8M(2)	0.222	0.308	0.282 / 0.245	0.213
8M(3)	0.275	0.331	0.297 / 0.296	0.251
8M(4)	0.247	0.308	0.267 / 0.256	0.227
9M(1)	0.263	n/a	n/a	n/a
9M(2)	0.331	0.386	0.345 / 0.314	0.268
10M(1)	0.135	0.162	0.149 / 0.143	0.133
10M(2)	0.142	n/a	n/a	n/a
10M(3)	0.147	n/a	n/a	n/a
-10M(1)	0.140	0.171	0.150 / 0.154	0.139
-10M(2)	0.144	n/a	n/a	n/a

Table 3(a). Heat transfer coefficients for prism faces averaged over entire visible space area and rotation cycle. Values are in Watts/cm²/°C.

Table 3 is split to present data from the prism faces (table 3a) and pyramidal faces (table 3b) separately. Faces are numbered as shown in figure 13. Data are not available for all sides and all cases. In cases 1, 2, and 5,

data for sides marked with (b) could not be obtained due to heater board burnouts. In cases 6M-10M, data for sides marked with (n/a) were not acquired due to time constraints. As shown in figure 13, portions of sides 1 and 5 were viewed separately by the +120° and -120° camera positions. Data from the two camera positions were averaged separately, and so the columns for sides 1 and 5 contain two values, one for each camera position. The camera which sees side 4 provides the first value in the column for side 1, while the camera which sees side 2 provides the second value, and similarly for the pyramidal faces. In cases 6M-10M, multiple runs of the same case are available. The separate runs are indicated by a number in parentheses after the case number.

Case	Side			
	7	8	5	6
1M	b	0.286	0.298 / 0.324	b
2M	b	b	0.336	b
3M	0.246	0.315	0.355 / 0.308	0.274
4M	0.308	0.292	0.315 / 0.360	0.313
5M	0.191	0.198	0.198 / 0.201	0.192
6M(1)	0.221	0.236	0.243 / 0.247	0.239
6M(2)	0.214	0.227	0.241 / 0.238	0.230
7M(1)	0.238	n/a	n/a	n/a
7M(2)	0.236	n/a	n/a	n/a
8M(1)	0.182	0.186	0.189 / 0.175	0.184
8M(2)	0.192	0.226	0.219 / 0.190	0.196
8M(3)	0.233	0.239	0.230 / 0.224	0.225
8M(4)	0.229	0.221	0.211 / 0.201	0.205
9M(1)	0.233	n/a	n/a	n/a
9M(2)	0.285	0.275	0.269 / 0.242	0.242
10M(1)	0.128	0.130	0.135 / 0.127	0.129
10M(2)	0.130	n/a	n/a	n/a
10M(3)	0.138	n/a	n/a	n/a
-10M(1)	0.133	0.138	0.134 / 0.139	0.135
-10M(2)	0.136	n/a	n/a	n/a

Table 3(b). Heat transfer coefficients for pyramid faces averaged over entire visible space area and rotation cycle. Values are in Watts/cm²/°C.

Heat transfer measurement variability: There is a significant degree of overlap between cases which allows an assessment of the variability of the heat transfer measurements. Specifically,

1. Within a given case, values for sides 1 and 5 generated by the two different camera positions should not differ significantly, and
2. Symmetry dictates that sides 2 and 4 see the same flow, and should have the same heat transfer coefficient, as will sides 6 and 8.

Table 4 shows the variation between values measured at these nominally identical conditions. The columns of

table 4 show the per cent variation from the mean values for the separate measurements of sides 1 and 5, and for sides 2-4, and 8-6.

Case	Parameter				
	Heat Rate	Side 1	Sides 4-2	Side 5	Sides 8-6
1M	1.18	-7		-8	
2M	1.19				
3M	0.51	20	13	14	14
4M	0.51	-13	-14	-13	-7
5M	0.39	14		-2	
6M(1)	0.92	-2	6	-2	-1
6M(2)	1.35	0	0	1	-1
7M(1)	0.93				
7M(2)	1.45				
8M(1)	0.99	5	25	6	1
8M(2)	1.03	14	36	14	14
8M(3)	1.05	0	27	3	6
8M(4)	1.03	4	30	5	8
9M(1)	1.01				
9M(2)	1.04	9	36	11	13
10M(1)	1.02	4	20	6	1
10M(2)	1.02				
10M(3)	1.02				
-10M(1)	1.02	-3	21	-4	2
-10M(2)	1.02				

Table 4. Variations in averaged heat transfer coefficients between faces where measurements are expected to be identical. Values in % except heat rate column, which is in Watts/cm².

In general, the second set of measurements (Cases 6M to 10M) show more consistent results than the first set. Two exceptions to this statement are case 8M(2) and the side 4-2 variation for all the 15 cm model cases (Cases 8M to 10M). Case 8M(2) shows a high variation which may indicate a camera problem while taking this case, although none was noted during data collection. In all the 15 cm cases, side 2 has a lower heat transfer coefficient than side 4, while in all the 30 and 60 cm cases, sides 1, 2, and 4 have broadly comparable heat transfer coefficients. This suggests that the side 2 data for the 15 cm crystal may be bad overall, possibly due to a manufacturing defect in the side 2 heater.

Compared to the second set of measurements, the first set (Cases 1M through 5M) have higher variation. Not enough data exist for cases 1M and 2M, the first set of measurements on the 30 cm crystal, to evaluate the level of variation in the measurements. The variability in measurement for the 60 cm crystal case is likely due to two factors. Due to the large crystal area, the heating rate for this crystal was lower than for the 30 cm and 15

cm models. In addition, the paint calibration results indicated that the paint used for this model had low sensitivity compared to other paint applications. Thus the TSP brightness change between heat-on and heat-off conditions is reduced, and this degrades the accuracy of the TSP measurement. Excluding case 8M(2) and side 2 for the 15 cm crystal, the mean variation between nominally identical sides is 6.4%, with a maximum variation of 20%.

Case	Side			
	3	4	1	2
1M		22	21 / 27	
6M(2)	-2	-5	0 / -2	-10
7M(2)	-3			
8M(1)	-17	-15	-12 / -13	-11
8M(2)	-10	0	6 / -4	-6
8M(3)	11	7	11 / 16	11
9M(2)	26			
10M(1)	-5			
10M(2)	4			
-10M(2)	3			

Table 5(a). Variation between heat transfer coefficients of prism sides for nominally identical cases. One case is arbitrarily chosen as a reference. Values are in %.

Case	Side			
	7	8	5	6
1M		21	23 / 31	
6M(2)	-3	-4	-1 / -4	-4
7M(2)	-1			
8M(1)	-21	-16	-12 / -13	-10
8M(2)	2	8	9 / 11	10
8M(3)	2	8	9 / 11	10
9M(2)	22			
10M(1)	-2			
10M(2)	6			
-10M(2)	2			

Table 5(b). Variation between heat transfer coefficients of pyramid sides for nominally identical cases. One case is arbitrarily chosen as a reference. Values are in %.

For some cases repeat runs exist, and it is possible to compare data taken for each side. For each set of comparable cases, the results for case were chosen to be the reference, and the deviation of the other cases from the reference is shown in Table 5. Note that cases 1M and 6M, and 2M and 7M, were taken at nominally identical conditions. There is generally good agreement between the different runs of case 6M, 7M and (for the limited data available) 10M. In particular, it should be

noted that different runs of cases 6M and 7M have significantly different heating rates. (Heating rates shown in table 4.) This indicates that changes in heating rate do not bias the measurement even though the lower heating rate used for cases 3M-5M may have increased measurement variability. However there is significant variation from run to run within cases 8 and 9. The cause for this variation is unknown.

Conversion of heat transfer to mass transfer:

Conversion factors between heat and mass transfer can be found using either equation 9 or 10. In this experiment the conversion factor k_c/h was found to be $6.2 \times 10^{-9} \text{ m}^3 \cdot \text{K}/\text{J}$ for the 15 and 30 cm model cases, and $3.3 \times 10^{-9} \text{ m}^3 \cdot \text{K}/\text{J}$ for the 60 cm model cases. These conversion factors imply that mass transfer coefficients range from $8.1 \times 10^{-6} \text{ m/s}$ to $2.2 \times 10^{-5} \text{ m/s}$ for the 15 and 30 cm model cases, and $6.3 \times 10^{-6} \text{ m/s}$ to $1.3 \times 10^{-5} \text{ m/s}$ for the 60 cm model cases, which are broadly consistent with observations of the full scale experiments.

Trends in averaged heat transfer coefficients: Trends in the time- and space-averaged data were examined by first generating an average value for each face. Sides 2 and 4 were averaged together, as were both measurements on side 1, to produce a single average value for each face. Then repeat runs for each case were averaged. (Exceptions: Case 8M(2) was dropped and only side 4 data was used for cases 8M-10M.) Figure 17 shows the heat transfer coefficients for each case sorted by side, for the prism sides only. Data for the pyramid sides are similar. Only the 60 cm cases show any significant difference from side to side. The 30 cm cases show some slight tendency towards lower heat transfer coefficient on side 3. The 15 cm cases and the continuous rotation cases show the least variation in heat transfer coefficient from side to side.

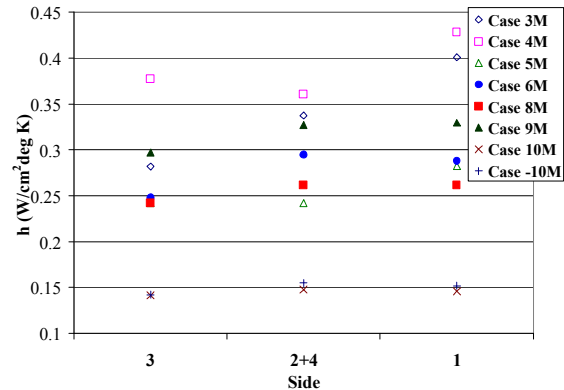


Figure 17. Heat transfer coefficients of prism sides sorted by side.

Since there appeared to be no significant variation in heat transfer from side to side, other trends were

evaluated by averaging results for all four sides. The results are shown for both the prism and pyramid faces in table 6, arranged by rotation rate and model size. In general faster rotation rate and larger model size result in higher heat transfer coefficients. Heat transfer coefficients on the pyramid faces are only 76-91% of the values attained on the prism faces, with a mean of 84%

	Rotation Rate		
Model Size	Slow	Fast	Continuous
15 cm	0.256	0.318	0.147
30 cm	0.277	0.269	
60 cm	0.340	0.389	0.256

Table 6(a). Heat transfer coefficients averaged over all four prism faces. Values are in Watts/cm²/°C.

	Rotation Rate		
Model Size	Slow	Fast	Continuous
15 cm	0.210	0.258	0.133
30 cm	0.231	0.237	
60 cm	0.291	0.316	0.195

Table 6(a). Heat transfer coefficients averaged over all four pyramid faces. Values are in Watts/cm²/°C.

Space-averaged, time-resolved results: As figure 16 shows, heat transfer coefficient varies significantly with time. The variation in spatially-averaged heat transfer coefficient for a representative case is shown in figure 18. Trends in heat transfer with time can be understood by referring to the velocity time history of figure 16. At $t=0$ and $t=13$ sec, the model has reversed direction and is accelerating into flow which is still rotating in the opposite direction. Heat transfer increases rapidly with the model rotation rate. Once the rotation rate reaches its “cruise” value, heat transfer slowly decreases as the bulk of the fluid accelerates to catch up with the model. As the model decelerates, heat transfer drops rapidly because the model is “backing” into previously heated fluid.

However, this simple picture is complicated by the time-resolved results for the continuous cases. Figure 19 shows time-resolved heat transfer coefficients for case 10M. The heat transfer coefficient does not settle to a constant value. Instead it appears to vary with a roughly 40 second time period. The data shown in figure 19 is representative – other runs of case 10, as well as other sides of the model, show the same variation. The origin of the time axis in figure 19 is misleading, since $t=0$ represents the time at which heating was turned on, not the start of rotation. Heat-off images had been acquired over a period of about 75

seconds prior to the start of heating, so the model had been in continuous rotation at about 1.9 revs/sec for roughly 98 seconds before the first heat-on data point was taken.

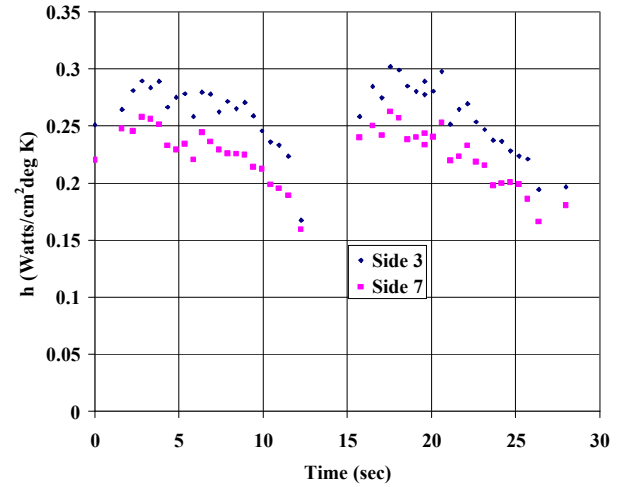


Figure 18. Spatially-averaged heat transfer coefficients for case 6M(1).

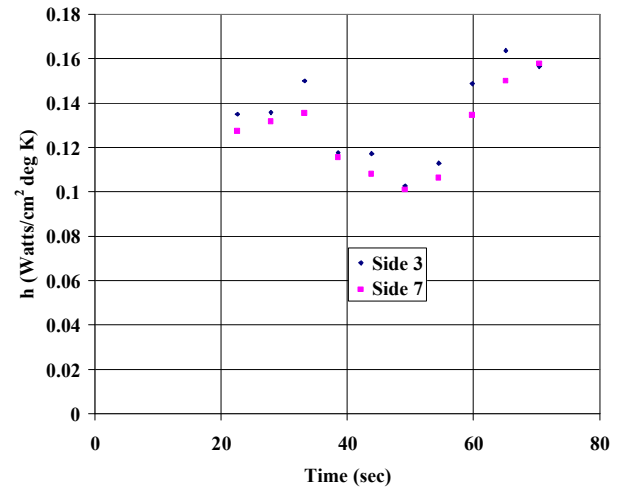


Figure 19. Spatially-averaged heat transfer coefficients for case 10M(1).

Temperature coefficient of resistance measurements: The time-resolved TSP results suggested that some useful data might be obtained from a time-resolved, spatially-averaged method of measuring the heat transfer coefficient. In the model experiment, mean surface temperature can be determined by monitoring the resistance of the heater boards, since the resistance of copper varies with temperature. To perform this experiment, the AC power supply used to drive the heater boards for the TSP measurements was replaced with a precision DC power supply, and high-precision volt and ammeters were used to measure the voltage

across and current through the model. Figure 20 verifies that there is significant time variation in the heat transfer coefficient of a crystal model in continuous rotation. The variation of heat transfer coefficient has a period of approximately 36 seconds, which is consistent with the ~ 40 second period observed in the TSP data. It should also be noted that the mean heat transfer coefficient for the model, of roughly $0.065 \text{ W/cm}^2 \text{ }^\circ\text{K}$, is only about 45% of the mean value as measured by the TSP. The reason for this discrepancy is not known.

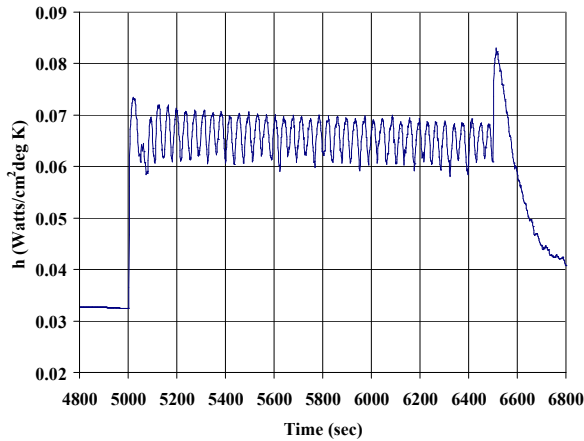


Figure 20. Time-resolved, spatially-averaged heat transfer coefficient for 15 cm model. Continuous rotation at 2 revs/sec begins at $t=5000$ sec and ends at $t=6500$ sec.

CONCLUDING REMARKS

Heat transfer coefficient measurements have been made on rotating model in a water bath in order to estimate mass transfer coefficients on a geometrically-similar crystal of KDP growing in a solution. Heat transfer measurements were made with temperature-sensitive paint at two different rotation rates for each of three different model sizes. An additional two cases were obtained with continuous model rotation.

The time-resolved TSP measurements, as well as the TSP images, show that there is considerable point-to-point variation of heat transfer coefficient over a rotation cycle. The data indicate that the highest heat transfer coefficients occur when the model is accelerating through fluid moving in the opposing direction. Once the model reaches its “cruise” rotation rate, a stable vortex structure rapidly (within a few revolutions) forms and co-rotates with the model. The vortex structure traps heated fluid and causes a slow decline in heat transfer coefficient as the model continues to rotate. This effect is probably more significant on the pyramid faces since they appear to be more directly exposed to the vortical flow. Measurements in the continuous rotation cases indicate

that if the “cruise” rotation rate was held indefinitely the heat transfer coefficient would decrease to about 60% of its peak value as the vortex structure stabilized. However in the normal course of a rotation cycle the model rotation reverses, breaking up the vortex structure. This returns the heat transfer coefficient to its peak value, but not before reducing it sharply as the model backs through the already-heated vortex structure.

When heat transfer coefficients are averaged over an entire face and rotation cycle, there is little variation from face to face. The largest variation is found in the 60 cm scale model crystal, which would be expected to have the largest degree of interaction with the rotation platform’s fins. When different crystal models and rotation rates are compared, heat transfer coefficient is found to increase with model size and rotation rate.

Mass transfer coefficients for the full scale conditions were calculated using the Chilton-Colburn analogy. Computed mass transfer coefficients were broadly in line with expectations from the full-scale crystal growth experiments. However, the question of whether the Chilton-Colburn analogy is appropriate for rotating models remains unclear.

It was found that continuous rotation does not result in a constant heat transfer coefficient over the model. Instead, the spatially-averaged heat transfer coefficient develops a stable oscillation around a steady state value, with a period roughly 18 times the revolution period. TSP images suggest that the stable vortex structure on the crystal is being periodically destroyed and recreated. This oscillation may be related to an interaction between the four-fold symmetry of the model and the three-fold symmetry of the rotation platform

This paper does not resolve the question of whether NIF crystal growth is dominated by kinetics or mass transfer coefficient. If the latter is the case, however, it is worthwhile to consider how mass transfer coefficient can be maximized. The time-resolved TSP measurements, as well as the TSP images, suggest some possible strategies. Prolonged rotation at a constant rate should be avoided, since this allows the generation of a stable vortex structure which reduces the spatially-averaged mass transfer coefficient. The vortex structure begins to develop within only a few rotations of the crystal. Within about 18 rotations, the vortex structure destabilizes and reforms, but the mass transfer coefficient will not regain its original values. Rapid deceleration should also be avoided, as this allows the crystal to back into solute-depleted flow behind it, and leads to a sudden sharp depression in mass transfer

coefficient. It is possible that mass transfer coefficient would be maximized by a rotation schedule that continuously varied rotation rates to avoid the formation of vortex structures without ever decelerating sharply enough to generate an abrupt dip in mass transfer coefficient.

¹ Rebecca Dylla-Spears, 2004, private communication

² Bell JH, Schairer ET, Hand LA, Mehta RD. 2001 Surface Pressure Measurements Using Luminescent Coatings. In Annu. Rev. Fluid Mech., vol. 33, pp. 155-206.

³ Liu T & Sullivan JP 2004 Pressure and Temperature Sensitive Paints (Experimental Fluid Mechanics), Springer-Verlag, Berlin.

⁴ Thorsness C, Land T, Dylla-Spears R, Ehrmann P, 2004 Recent KDP Large Boul Runs – Congruent Growth, Lawrence Livermore National Laboratory memo, NIF0111317, Sept., 15.

⁵ DeYoreo JJ, Burnham AK, Whitman PK, 2002, “Developing KH_2PO_4 and KD_2PO_4 crystals for the world’s most powerful laser, *International Materials Review* 47(3), 113-152 (2002).